Journal of Colloid and Interface Science 336 (2009) 842–849

Contents lists available at ScienceDirect

Journal of Colloid and Interface Science

www.elsevier.com/locate/jcis

Rheology of the Pluronic P103/water system in a semidilute regime: Evidence of nonequilibrium critical behavior

V.V.A. Fernández [a], N. Tepale [a,c], J.G. Álvarez [a], J.H. Pérez-López [a], E.R. Macías [a], F. Bautista [b], F. Pignon [c], Y. Rharbi [c], R. Gámez-Corrales [d], O. Manero [e], J.E. Puig [a], J.F.A. Soltero [a,c,*]

[a] Departamento de Ingeniería Química Universidad de Guadalajara, Boul. M. García Barragán # 1451, Guadalajara, Jal. 44430, Mexico
[b] Departamento de Física, Universidad de Guadalajara, Boul. M. García Barragán # 1451, Guadalajara, Jal. 44430, Mexico
[c] Laboratorie de Rhéologie, Université Joseph Fourier Grenoble I, Institut National Polytechnique de Grenoble, CNRS, UMR 5520, B.P.53, F-38041 Grenoble Cedex 9, France
[d] Departamento de Física, Universidad de Sonora, Apdo. Postal #130, Hermosillo, Sonora 83000, Mexico
[e] Instituto de Investigaciones en Materiales, Universidad Nacional Autónoma de México, Apdo. Postal 70-360, México, D.F. 04510, Mexico

ARTICLE INFO

Article history:
Received 6 December 2008
Accepted 27 February 2009
Available online 9 April 2009

Keywords:
Worm-like micelles
Shear-banding flow
BMP model
Extended irreversible thermodynamic
Nonequilibrium critical phenomenon

ABSTRACT

The linear and nonlinear rheological behaviors of semidilute aqueous solutions of the amphiphile triblock polymer Pluronics P103 in water are reported here. For $C_{surf} \leqslant 20$ wt%, micelles are spherical at temperatures lower than ca. 27 °C and grow with increasing temperature to form long polymer-like micelles. These polymer-like micelles exhibit strong viscoelasticity and a shear-banding region that shrinks as the cloud point is approached. Master time–temperature–concentration curves were obtained for the dynamic moduli using traditional shifting factors. In the nonlinear regime, P103 polymer-like micellar solutions follow the master dynamic phase diagram proposed by Berret and colleagues, in which the flow curves overlap in the low-shear-rate homogeneous flow region. Within the nonhomogeneous flow region (confirmed by flow birefringence and small-angle light-scattering measurements), oscillations and overshoots are detected at the inception of shear flow, and two main relaxation mechanisms are apparent after cessation of steady shear flow. Evidence for nonequilibrium critical behavior is presented, in which the order parameter is the difference of critical shear rates that limit the span of the plateau stress. Most of the steady-state and transient features of the nonlinear rheology of the P103 polymer-like micelles are reproduced with the Bautista–Manero–Puig (BMP) model, including the predictions of nonequilibrium critical behavior under flow.

1. Introduction

Pluronics are amphiphilic triblock copolymers denoted by $(PEO)_n(PPO)_m(PEO)_n$, where n and m represent the number of hydrophilic poly(ethylene oxide) (PEO) and hydrophobic poly(propylene oxide) (PPO) units, respectively. These nonionic surface-active polymers have been attracting attention for their potential use as controlled drug-delivery agents [1–3].

Due to their amphiphilic character, Pluronics are capable of forming micelles in water [1–3]. At low Pluronic concentrations, spherical micelles grow progressively to form polymer-like micelles (or worm micelles) as the temperature is increased. This transition was reported in aqueous solutions of Pluronic P85 [4–7] and P84 [8–12]. This micellar growth is characterized by a drastic viscosity increase of about five orders of magnitude [9,12]. Likewise, when the length of the polymer-like micelles and the entanglement number density augment on increasing temperature, the oscillatory shear storage modulus G' increases rapidly, attaining a gel-like behavior [13–17]. Shear-banding flow has been observed by small-angle X-ray scattering (SAXS) and rheometry in micellar cubic crystals of the F68/water system [18,19] and by small-angle light-scattering (SALS) and rheological measurements in dilute aqueous solutions of the copolymer P84 [12]. The shear-banding flow observed in triblock copolymer solutions has features similar to those in polymer-like micellar solutions of ionic surfactants [20–23].

Álvarez-Ramírez and co-workers studied the phase behavior of the P103/water system using density and ultrasound velocity measurements, DSC, light scattering, and rheology [24]. They reported that the critical micellar temperature (CMT) decreases as concentration increases. Above the CMT and for temperatures up to 40 °C and concentrations up to ca. 22 wt%, a clear micellar (L_1) phase is formed. In this concentration range the cloud point temperature (CPT) is detected at ca. 41 °C.

Here, the linear and nonlinear rheological behaviors of semidilute aqueous micellar solutions of P103 are investigated as functions of temperature and concentration. In the linear regime, the dynamic moduli do not follow Maxwell behavior with a single

* Corresponding author.
E-mail addresses: jfasm@hotmail.com, armandosolteros@yahoo.com (J.F.A. Soltero).

0021-9797/$ - see front matter © 2009 Elsevier Inc. All rights reserved.
doi:10.1016/j.jcis.2009.02.064

relaxation time but time–temperature–concentration master curves can be obtained using classical shifting factors. In the nonlinear regime, a stress plateau is observed between two critical shear rates in a narrow temperature range. Data allow examinaton of the critical behavior under flow, in which a critical point, a critical isotherm, and spinodal and coexistence lines are determined. The steady-state and transient nonlinear viscoelastic responses in the phase diagram region where polymer-like micelles form are compared with the predictions of the BMP model [25–27]. This model is unique since it predicts quantitatively the steady and transient nonlinear rheology of complex fluids that break and reform under flow such as worm-like micellar solutions and slurries [25–31]. Moreover, it predicts the long transients and times to achieve steady state in the nonhomogeneous state. The shear-banding flow is analyzed here by birefringence and SALS measurements under shear flow and rheometry. More importantly and even though shear-banding flow has been observed in other Pluronics/water systems [12,18,19], this is the first time that experimental data and model predictions of shear banding presented here are associated with a nonequilibrium phase transition and they reveal the existence of an out-of-equilibrium critical point.

2. Modeling

The model employed here consists of the upper-convected Maxwell constitutive equation coupled to a kinetic equation that accounts for the breaking and reformation of micelles [25,26,32]. Since this model is able to reproduce the master dynamic phase diagram proposed by Berret et al. [33], the dimensionless shear stress ($\bar{\sigma}_{12} = \sigma_{12}/G_0$) and shear rate ($\bar{\dot{\gamma}}_{12} = \tau_R\dot{\gamma}_{12}$) are employed here, where G_0 is the plateau shear storage modulus and τ_R is the main relaxation time, determined from the inverse of the crossover frequency of the storage and loss moduli in linear oscillatory measurements. However, as detailed below, G_0 was estimated (since it was not observed) as the ratio of η_0 and τ_R, where η_0 is the zero-shear-rate viscosity. For simple-shear flow and after neglecting normal stress differences since normal stresses are not examined here, the dimensionless model reduces to the following system of ordinary differential equations:

$$\bar{\sigma}_{12} + \frac{1}{\bar{\varphi}}\frac{d\bar{\sigma}_{12}}{d\bar{t}} = \frac{1}{\bar{\varphi}}\bar{\dot{\gamma}}_{12} \tag{1}$$

$$\frac{d\bar{\varphi}}{d\bar{t}} = \frac{(1-\bar{\varphi})}{\bar{\tau}_e} + \bar{k}_0(1+\bar{\upsilon}\bar{\dot{\gamma}}_{12})(\bar{\varphi}_\infty - \bar{\varphi})\bar{\sigma}_{12}\bar{\dot{\gamma}}_{12} \tag{2}$$

Here $\bar{t} = t/\tau_R$ is the dimensionless time, $\bar{\varphi} = \bar{\dot{\gamma}}_{12}/\bar{\sigma}_{12}$ is the dimensionless fluidity or inverse of the dimensionless shear viscosity $\bar{\eta}$. The dimensionless model constants are defined as $\bar{k}_0 = G_0 k_0$, $\bar{\tau}_e = \tau_e/\tau_R$, $\bar{\upsilon} = \upsilon/\tau_R\bar{\varphi}_\infty = G_0\tau_R\varphi_\infty = \varphi_\infty/\varphi_0$, where φ_0 and φ_∞ are the fluidity at zero and infinite shear rate, respectively, τ_e is a structure reformation time, k_0 is a kinetic constant for structure breakdown, and υ is the *shear-banding intensity* parameter.

For steady simple-shear flow, Eqs. (1) and (2) with their time derivatives set to zero give

$$\bar{\varphi}^2 - \bar{\varphi} - \bar{k}_0\bar{\tau}_e(\bar{\varphi}_\infty - \bar{\varphi})\bar{\dot{\gamma}}_{12}^2(1+\bar{\upsilon}\bar{\dot{\gamma}}_{12}) = 0. \tag{3}$$

The model requires six parameters to predict experimental data, φ_0, φ_∞, G_0, k_0, τ_e, and υ, although at steady state the dimensionless model requires only three of them. All of them, except υ, can be estimated from independent rheological experiments as described elsewhere [25]. The shear-banding intensity parameter υ is uniquely determined from the value of the stress at the plateau region, which can be estimated from the minima in the dissipated or extended Gibbs free energy ($\mathscr{G}$) of the two stable branches as determined by an extended irreversible thermodynamics (EIT) analysis [26,32]. It can be shown, following Bautista et al. [26,32], that for polymer-like micelles under shear flow and after neglecting normal stresses, the dissipated energy is given by

$$d\mathscr{G} = \left(\frac{v}{\tau_R\varphi_0}\right)\bar{\sigma}_{12}d\bar{\dot{\gamma}}_{12}, \tag{4}$$

where v is the specific volume. Substitution of the steady-state version of Eq. (1) in Eq. (4) and integration give

$$\Delta\mathscr{G} = \frac{v}{\tau_R\varphi_0}\int\frac{\bar{\dot{\gamma}}_{12}}{\bar{\varphi}}d\bar{\dot{\gamma}}_{12}, \tag{5}$$

where $\bar{\varphi}$ is the solution of Eq. (3).

Inasmuch as the working equations are written in terms of the dimensionless shear stress and shear rate, subscripts in these two variables will be dropped in the rest of the paper for simplicity.

3. Experimental

Pluronic P103 [$(EO)_{17}(PO)_{60}(EO)_{17}$], from BASF, was used as received. Water was drawn from a Millipore purification system. Samples were prepared by weighing appropriate amounts of P103 and water in 30-mL vials. The vials were placed in a water bath at 30 °C for a week, where they were frequently shaken to speed up homogenization. Then samples were allowed to reach equilibrium at the measurement temperature. All samples were centrifuged to remove suspended air bubbles before being tested. To avoid light degradation of the samples, the vials were covered with aluminum foil.

Steady, unsteady, and oscillatory simple-shear experiments were performed in a TA Instruments Ares-22 rheometer with cone-and-plate geometry of 0.1 rad and 50 mm in diameter. Frequency sweeps were made at oscillatory strain deformations within the linear viscoelastic region, which is defined as that where the storage (G') and the loss (G'') moduli are strain independent. An environmental control unit was placed around the cone-and-plate fixture to prevent water evaporation. Temperature was controlled within 0.1 °C during measurements.

SALS measurements under shear flow were performed at 36 °C in a home-made device with parallel-plate geometry (Fig. 1). The laser test facility used for the experiment was developed and built as described elsewhere [34]. It consists of a 2 mW laser beam (He–Ne) with a wavelength λ = 632.8 nm and a Fresnel lens acting as scattering screen. The detector is a video camera with a CCD 752*582 pixel sensor. Image processing analysis was performed with a video system and specific software. The scattering patterns were recorded by the camera and video system throughout the test. The modulus of the scattering vector is given by q=[$(4\pi n/\lambda)$ sin(θ/2)], where n is the refractive index of the suspending

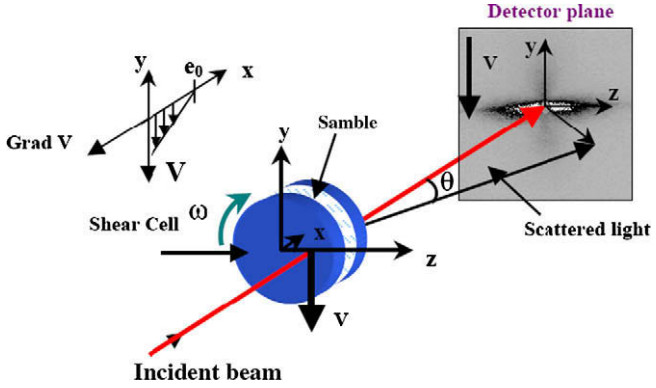

Fig. 1. Schematics of home-built device for SALS measurements under shear.

medium, λ the wavelength of the radiation, and θ the scattering angle. The light-scattering measurements cover a q-range from 2×10^{-5} to 4×10^{-4} Å^{-1}. A parallel-plate cell was built to observe the structure during flow [35,36]. The sample, which has a fixed thickness (e_0) of 0.3 mm, is sheared between two parallel quartz disks, one of which rotates at an angular rotation speed ω around the x-axis. The light beam is directed along the x-direction, parallel to the axis of rotation and perpendicular to the disks lying in the y–z plane at a point along the horizontal z-axis, located at a distance R_c from the axis of rotation. The local tangential velocity $\mathbf{V} = -vy$ is collinear to the y-axis (see Fig. 1). The detector records the intensity of light scattered by the sample in the y–z plane (velocity–vorticity plane). Consequently, the plane of observation corresponds to the y–z plane. The shear plane is parallel to the x–y plane (gradient–velocity plane) and the local shear rate at a given distance R_c is $\dot{\gamma} = R_c\omega/e_0$. The cell is airtight, which prevented water evaporation of the samples. To control the sample temperature, the shear cell is positioned in a box with an air control temperature setup conducted by a PID system. The temperature of the sample is measured with a K-thermocouple positioned in the stainless-steel blade, which maintains the quartz glass disks in contact with the sample. All measurements were done at 36(±0.5) °C. Some measurements were performed on a TA Instruments ARES-22 rheometer with exactly the same quartz glass parallel-plates geometry used for the light-scattering measurements to assess that no wall slip occurs. The level of stress is in good agreement with that measured using the other steel tools.

4. Results

Fig. 2 depicts the zero-shear-rate viscosity (η_0) as a function of temperature for a 20 wt% P103 solution. For temperatures between 18 and 25 °C, η_0 is ca. 200 times the water viscosity and fairly independent of temperature. At about 26–27 °C, η_0 begins to rise signaling the critical entanglement concentration (c^*) and continues to increase rapidly up to ca. 30 °C, due to micellar growth. At even higher temperatures, η_0 keeps increasing but with a shallower slope up to the cloud point [24]. Note that η_0 increases more than three orders of magnitude in the temperature interval examined; concurrently, the solution becomes highly viscoelastic (see below). Interestingly, it takes very long times and oscillations to reach the steady-state η_0 value in the concentration range where the P103 micelles begin to grow (inset in Fig. 2). Below 26 °C, where micellar growth has not occurred yet, and above 37 °C, where polymer-like micelles already exists, steady state is reached rapidly without oscillations.

Fig. 3 shows frequency sweeps as a function of temperature made on a 20 wt% P103 sample. At low temperatures ($T < 33$ °C), where smaller polymer-like micelles form [24], the linear viscoelastic behavior (square and circles in figure) can be reproduced with the generalized Maxwell model with three relaxation times. In this low-temperature range, the crossover frequency occurs at $\omega > 100$ s^{-1}. With increasing temperature, the crossover frequency shifts to lower values because of the growth of the polymer-like micelles and the increasing number density of entanglements and five relaxation times are required to describe the linear viscoelastic behavior. At even higher temperatures, near the CPT, gel-like behavior is observed, i.e., $G' > G''$ in the whole frequency range examined. This behavior is opposite to that observed in polymer-like micellar solutions formed by ionic surfactants.

Fig. 4 shows the variation of G' and G'' versus frequency, measured at 36 °C, for various P103 concentrations. A strong dependence of the linear viscoelastic properties on concentration is evident. All the samples, except for the 25 wt% sample, exhibit a crossover of G' and G″ at a characteristic frequency (ω_c) in the examined frequency range; the reciprocal of this crossover frequency corresponds to the main relaxation (or disentanglement) time of the system τ_R. The crossover frequency ω_c shifts to lower values with increasing concentration (and with increasing temperature as shown in Fig. 3). Note that for concentrations higher than 20 wt% the chains are highly entangled, and hence a predominant elastic behavior is observed. It is important to remark that from ca. 15 to 23 wt% and temperatures between 30 and ca. 37 °C, P103 forms polymer-like micelles that break and reform like low molecular weight surfactant micelles. These systems exhibit a complex rheological behavior, which is controlled by either of two relaxation mechanisms, mainly, a kinetic-controlled or a diffusion-controlled relaxation mechanism [37]. The ratio of the breaking time to the reptation time ($\zeta = \tau_{Break}/\tau_{Rep}$) controls the relaxation of the system: for very small values of ζ, a single relaxation time dominates and near-Maxwell behavior follows whereas for larger values of ζ, a spectra of relaxation times and deviations from Maxwell behavior are observed, similar to polymer solutions with wide molecular weight distributions [37]. Here, Maxwell behavior is not observed in the whole concentration and temperature ranges where P103 form polymer-like micelles, which is evident from results depicted in Figs. 3 and 4 and from the early departures from

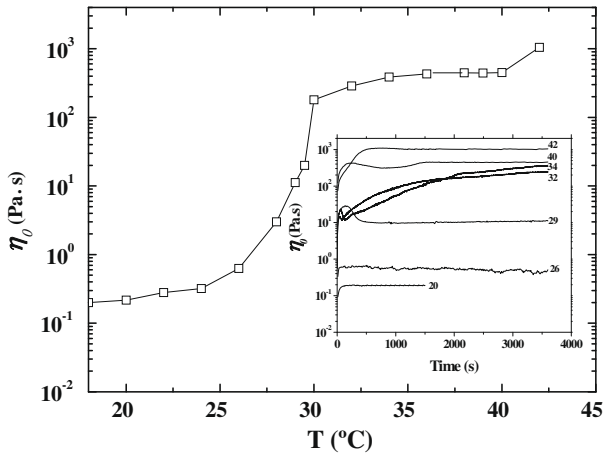

Fig. 2. Zero-shear-rate viscosity (η_0) as a function of temperature for a 20 wt% P103 solution. Inset: stress growth for a 20 wt% P103 aqueous solution.

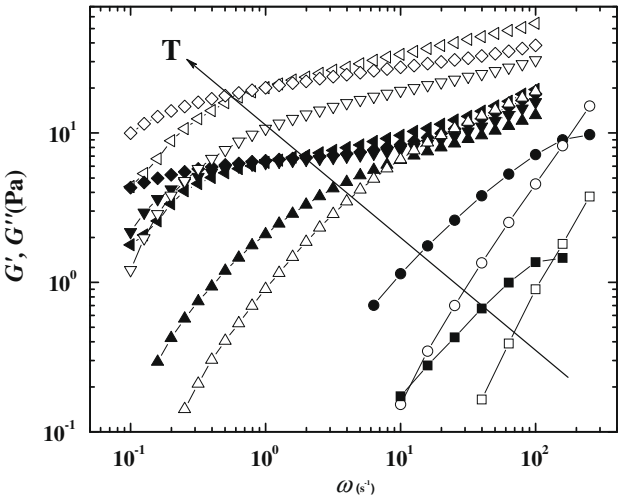

Fig. 3. Storage G' (open symbols) and loss G'' (closed symbols) moduli versus frequency for a 20 wt% P103 aqueous solution measured at different temperatures (°C): (□) 30; (○) 32; (△) 34; (▽) 36; (◇) 38; and (◁) 40.

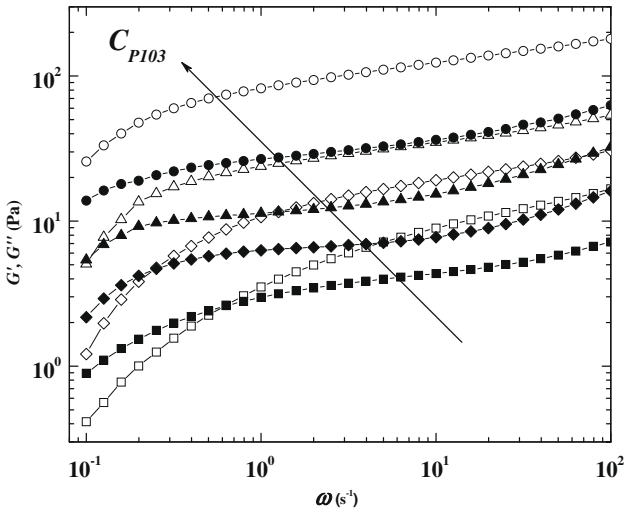

Fig. 4. Storage G' (open symbols) and loss G'' (closed symbols) moduli versus frequency measured at 36 °C for various P103 aqueous solutions (wt%): (□) 15; (◇) 20; (△) 22.5; (○) 25.

the osculating semicircle in Cole–Cole plots (not shown), indicating that the relaxation is diffusion controlled. Waton et al. [12] observed similar linear rheological behavior in P84 polymer-like micelles, indicating that these systems are *not* in the so-called *fast-breaking regime*.

Fig. 5 depicts time–temperature–concentration master plots of G' and G'' for P103 concentrations of 15, 17.5, and 20 wt% within a temperature range of 33 to 36 °C, which correspond to the region where polymer-like micelles form. Classical shifting factors were employed where the reference temperature was taken as 33 °C [38]. Data for the storage modulus (Fig. 5A) overlap in the whole concentration and temperature range examined. The loss modulus data also overlap at low frequencies, but they depart at higher reduced frequencies (Fig. 5B). These departures, which have also been reported in cationic surfactant worm-like micelles [20–23], are related to the breaking time of the micelles and to the onset of incidence of Rouse and breathing modes [39]. Note that as temperature is increased, the reduced separation frequency ($\omega^*\tau_R$) shifts to higher values; this behavior is the opposite of that observed in polymer-like micellar solutions of ionic surfactants [21,23]. Again, this is a consequence of the growth of the P103 micelles with temperature. The solid lines represent the fit of the generalized Maxwell model using five modes, the values of which are disclosed in Table 1.

Fig. 6 depicts steady shear master diagrams proposed by Berret et al. [33] for 15, 17.5, and 20 wt% P103 samples from 30 to 36 °C, which correspond to the temperature and concentration ranges where flexible polymer-like micelles form. At $\bar{\dot{\gamma}} < 0.5$, the behavior is Newtonian and all the data nearly collapse in a single line. For polymer-like micellar solutions of ionic surfactants, this region extends up to $\bar{\dot{\gamma}} = 1$ [21,23]. For $\bar{\dot{\gamma}} > 0.5$, where shear thinning appears, the data spread and the slopes of the flow curves diminish with increasing temperature in the intermediate shear-rate range, and they are almost flat for the highest temperatures examined. This quasi-stress plateau occurs at $\bar{\sigma} = 1.6$, which is higher than the value ($\bar{\sigma} = 0.67$) predicted by the Cates model for micellar systems [37].The presence of a stress plateau in micellar solutions and other complex fluids has been associated with the development of shear-banding flow between two critical shear rates ($\bar{\dot{\gamma}}_{c1}$ and $\bar{\dot{\gamma}}_{c2}$), which determine the onset and the end of the stress plateau [21,23]. For $\bar{\dot{\gamma}} > \bar{\dot{\gamma}}_{c2}$, the system exhibits a second Newtonian zone. The predictions of Eq. (3), shown as solid lines in Fig. 6, follow the

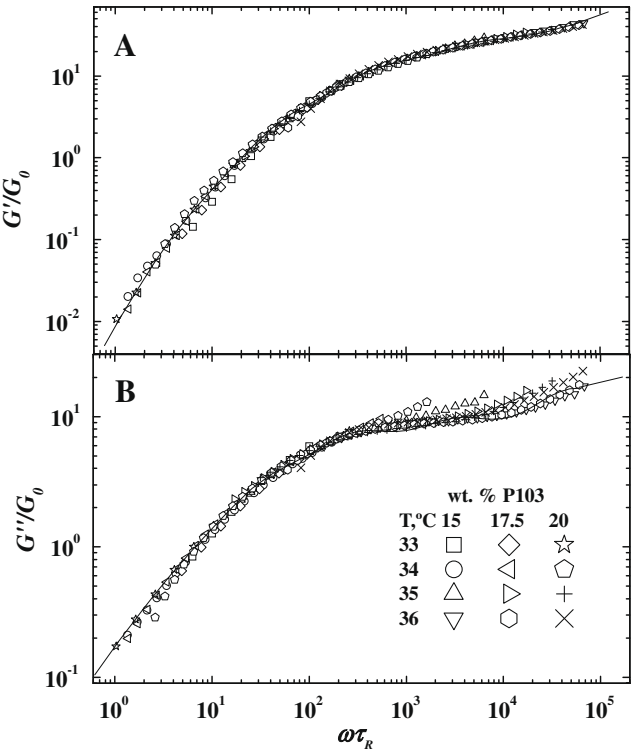

Fig. 5. Time–temperature–concentration superposition master curves for (A) G' and (B) G''. The solid lines are the best fits to the multimodel Maxwell model with five modes.

Table 1
Discrete viscoelastic spectrum obtained from the oscillatory measurements and the best fit with the generalized Maxwell model with 5 modes [37].

$G_{0(i)}$(Pa)	$\lambda_{0(i)}$(s)
31.4	0.0000168
13.9	0.0003
11.4	0.0032
3.9	0.023
0.3	0.15

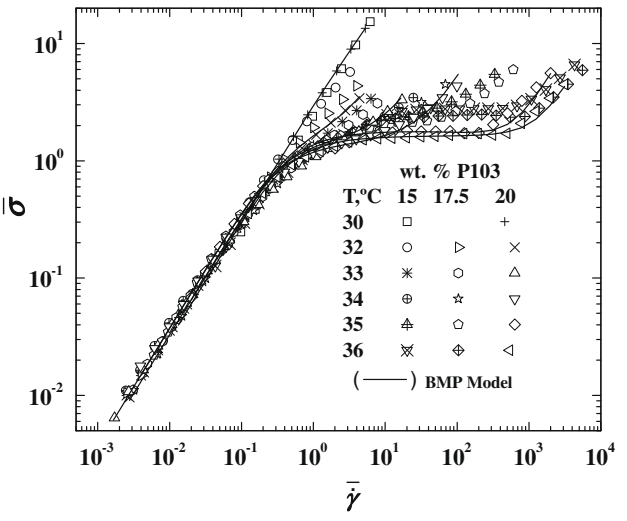

Fig. 6. Dimensionless shear stress versus dimensionless shear rate as a function of temperature and P103 concentration (wt%). Solid lines are the predictions of the BMP model with Eq. (3).

Table 2
Parameters of the BMP model obtained from independent rheological measurements.

T (°C)	$\bar{\dot{\gamma}}_{c1}$	$\bar{\dot{\gamma}}_{c2}$	φ_0 (Pa s)$^{-1}$	φ_∞ (Pa s)$^{-1}$	$k\tau_\lambda$ (s Pa)$^{-1}$	$\bar{\upsilon}$	G_0 (Pa)	τ_λ (s)	λ (s)
30	–	–	28.98	56.82	5	0.0001	2.33	–	0.011
32	–	–	3.83	27.29	2×10^{-4}	0.00015	19.43	0.05	0.006
33	–	–	1.43	21.33	2.1×10^{-4}	0.00017	12.21	0.058	0.008
34	6.1	55	0.035	22.69	4×10^{-4}	0.008	16.1	1.788	0.034
35	1.4	146	0.0331	35.1	44×10^{-4}	0.0097	8.22	4.055	1.082
36	1.7	357	0.0172	36.7	5×10^{-4}	0.011	7.13	7.02	3.81
38	–	–	0.0089	49.65	1.9×10^{-3}	–	–	–	–

experimental data quite well in the whole temperature and concentration ranges examined. The values of the parameters of the model are reported in Table 2.

Fig. 7 shows the constitutive curves for various values of the dimensionless shear-banding intensity parameter (Fig. 7A) and plots of the dissipated energy as functions of the dimensionless shear rate (Fig. 7B) for temperatures lower than (but near) the thermodynamic cloud point. Experimental data show clearly the transition from a discontinuous flow curve with a plateau into a monotonically increasing flow curve as temperature is increased (Fig. 7A). The curve corresponding to values such that $\bar{\upsilon}$ becomes nearly zero corresponds to the critical isotherm (or close to it since it is very difficult to find numerically a *critical point*, even an equilibrium one using a cubic equation of state). The constitutive curve depicts a region of negative slope bounded by the spinodal line (see Fig. 7A). The nonequilibrium dissipation energy (Fig. 7B) exhibits two minima of equal depth that become shallower as $\bar{\upsilon} \to \bar{\upsilon}_c$, i.e., as the plateau region disappears. Moreover, the minima in the dissipation equilibrium coincide with the critical shear rates, $\bar{\dot{\gamma}}_{c1}$ and $\bar{\dot{\gamma}}_{c2}$, that bound the plateau stress region. As the stress plateau region shrinks, the dissipation energy minima become nearly flat as the nonequilibrium critical point is approached (Fig. 7B). This quite flat $\mathcal{G}$ versus $\bar{\dot{\gamma}}$ curve implies that small energy fluctuations may produce strong shear-rate variations similar to density fluctuations around an equilibrium critical point. Moreover, for $\bar{\upsilon} > 0$, along the negative slope (see Fig. 7A), the system is unstable. As pointed out elsewhere [32], the system recovers stability by developing shear bands, the states of which correspond to various shear bands that have a dissipation energy curve with two minima of equal depth, which causes the coexistence of two bands supporting different shear rates, as shown in Fig. 7.

In time-dependent experiments, long transients and oscillations typically accompany shear-banding flow [20,40,41]. Fig. 8 depicts the stress growth after inception of shear flow for the 20 wt% sample at 36 °C measured at different applied shear rates. At shear rates within the low-shear-rate Newtonian region detected in steady shear measurements, the stress growth is monotonic and reaches its steady value within a few relaxation times of the sample. At shear rates prior to those where shear-banding flow develops, overshoots are observed. When experiments are performed in the shear-banded flow region, i.e., within $\bar{\dot{\gamma}}_{c1}$ and $\bar{\dot{\gamma}}_{c2}$, oscillations arise that last very long times. These transients and oscillations in the shear stress have been associated with the kinetics of nucleation and growth of a second phase, similar to phenomena reported in equilibrium first-order phase transitions [33]. For shear rates larger than $\bar{\dot{\gamma}}_{c2}$, where only the shear-induced phase exists, the oscillations disappear and the steady stress is again reached very rapidly. The predictions of Eqs. (1) and (2) of the BMP model using the experimental values of G_0 and τ_R obtained from linear oscillatory measurements reproduce the experimental data quite well in the low- and high-shear-rate Newtonian regions; however, in the shear-banding region, the predictions are only qualitative and hence, predictions are not displayed in this figure. The model does not predict oscillations but it predicts the shift of the first overshoot to shorter times as the applied shear rate is increased [20]. On the other hand, the stretched exponential form suggested by Berret et al. [42] fits the data well (predictions not shown).

A distinctive feature of shear banding is the development of two main relaxation times after cessation of steady shear flow when the applied shear rate is between $\bar{\dot{\gamma}}_{c1}$ and $\bar{\dot{\gamma}}_{c2}$, due to the formation

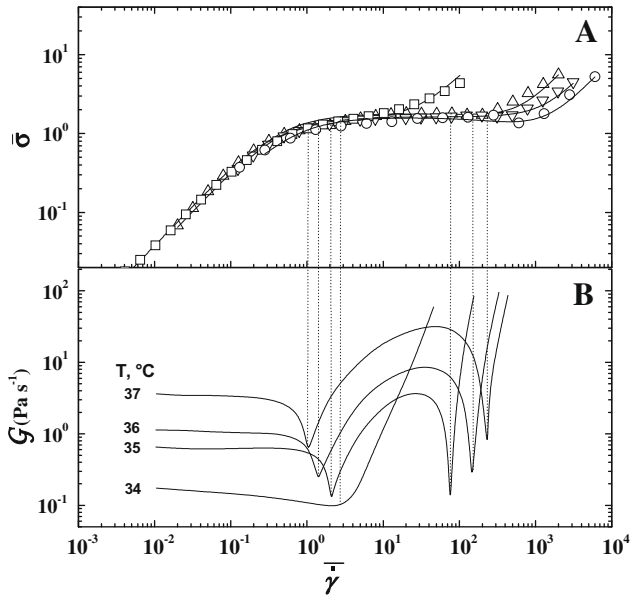

Fig. 7. Dimensionless shear stress (A) and dissipated energy (B) versus dimensionless shear rate for 20 wt. % P103 aqueous solutions at different temperatures (°C): (□) 34; (△) 35; (▽) 36; (○) 37. The solid lines are the predictions of the BMP model with Eqs. (3) (Fig. 7A) and (5) (Fig. 7B).

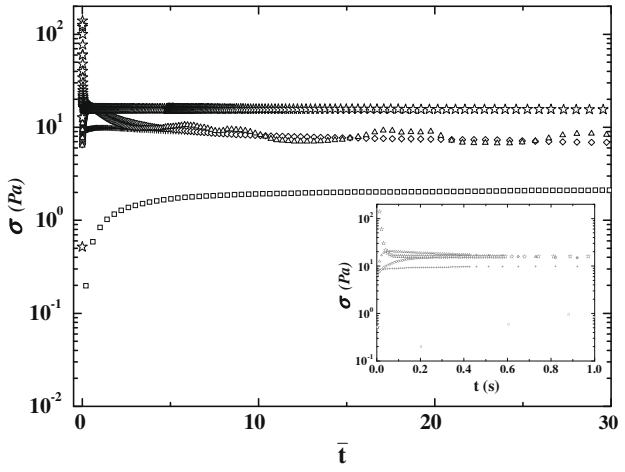

Fig. 8. Stress growth versus dimensionless time for a 20 wt% P103 aqueous solution at different applied shear rates (s^{-1}): (□) 0.03; (×) 0.1; (◇) 1.0; (△) 10; (☆) 500. Inset: stress growth at short times for a 20 wt% P103 aqueous solution at different applied shear rates.

of a second phase; for shear rates smaller than $\bar{\dot{\gamma}}_{c1}$ or larger than $\bar{\dot{\gamma}}_{c2}$, the relaxation is single exponential [28]. Fig. 9 depicts the normalized stress relaxation (σ/σ_{SS}, being σ_{SS} the steady shear stress prior to cessation of flow) versus the dimensionless time after cessation of steady shear flow as a function of the applied dimensionless shear rate for the 20 wt% P103 solution. For shear rates lower than $\bar{\dot{\gamma}}_{c1}$, i.e., within the low-shear-rate Newtonian region (shear rate indicated by A in inset), the relaxation is single exponential (curve A). When the shear rate is within the shear-banding region (indicated by B–E in inset), two main relaxation times are discernible (curves B–E) with a transition region between them. Note that the relaxation is single exponential in the homogeneous low-shear-rate Newtonian region (i.e., for $\bar{\dot{\gamma}} < \bar{\dot{\gamma}}_{c1}$) where only one structure exists, and it is multiexponential with two main relaxation times in the heterogeneous shear-banding flow region. Unfortunately, data could not be taken at shear rates where the second homogeneous flow branch appears, i.e., for $\bar{\dot{\gamma}} > \bar{\dot{\gamma}}_{c2}$. However, experimental data reported elsewhere for a cationic micellar solution [28] reveal that a single exponential with a slope similar to the fast relaxation in the shear-banding region is recovered when the high-shear Newtonian branch is attained. The similarities of the relaxation slope when $\bar{\dot{\gamma}}_{applied} < \bar{\dot{\gamma}}_{c1}$ with the slow mechanism and of the relaxation slope when $\bar{\dot{\gamma}}_{applied} > \bar{\dot{\gamma}}_{c2}$ with the fast relaxation mechanism suggest that the fast relaxation corresponds to the structure at the high-shear-rate branch and that the slow one corresponds to the structure of the low-shear-rate branch. Note that the slopes of the slow and the fast mechanisms increase as the applied shear rate is increased within the shear-banding region. We proposed that this is the effect of the disappearance of the lubricating band. For this situation, the BMP model gives

$$\sigma = \bar{\sigma}_{ss} \exp\left[-\left(\bar{t} + \bar{\tau}_e(\bar{\varphi}_{ss} - 1)\left(1 - e^{-\bar{t}}\right)\right)\right], \tag{6}$$

which has two limits. For short times, Eq. (6) reduces to

$$\bar{\sigma} = \bar{\sigma}_{ss} \exp\left[-\bar{\varphi}_{ss}\bar{t}\right], \tag{7}$$

and for long times, Eq. (6) yields

$$\bar{\sigma} = \bar{\sigma}_{ss} \exp\left[-(\bar{t} + \bar{\tau}_e(\bar{\varphi}_{ss} - 1))\right]. \tag{8}$$

These equations indicate that a short times, curves with different slopes for each steady state determined by $\bar{\varphi}_{ss}$ are predicted, whereas at long times, these curves should be nearly parallel (i.e., they present similar slopes) with intercept (at $t = 0$) depending on the steady-state fluidity. In fact, the predictions of the BMP model, shown in Fig. 9 as solid lines, reproduce the experimental data quite well in the single exponential as well as in the multiexponential relaxation regions with nearly parallel decays at long times.

Because the flow curve evolves from being monotonic ($T < 34$ °C) to nonmonotonic at intermediate temperatures and then monotonic again at higher temperatures ($T \geqslant 37$ °C) (see Fig. 7), stress relaxation measurements were performed in the 20 wt% P103 solution as a function of temperature at a fixed applied nondimensional shear rate ($\bar{\dot{\gamma}} = 10$) (Fig. 10); this dimensionless shear rate was chosen because it is within the shear-banding region at the intermediate temperatures and in the homogeneous flow regions at low and high temperatures (see inset A in Fig. 10). Note that as temperature increases, the relaxation evolves from a single decay to a multiexponential decay with two dominant modes at short and long times, and again to a single exponential decay at higher temperatures (see inset B in Fig. 10). It is noteworthy that: (1) the relaxation is single exponential when the applied shear rate corresponds to the homogeneous region and multiexponential when the applied shear rate falls within the stress plateau region, (2) the slopes of the single relaxation modes at low and high temperatures are similar to those of the low and fast relaxation modes at intermediate temperatures, (3) the slopes at short times differ whereas the slopes at long times are nearly parallel, and (4) in the dimensionless form, all curves within the shear-banding region nearly collapse at long times (cf. curve b–e with same curves in inset B). This suggest the existence of two structures in the stress plateau region: one which is akin to the low-temperature solution, and another which resembles more the rheological response of the higher temperature solution that is closer to the phase boundary. The predictions of the BMP model, shown in Fig. 10 as solid lines, follow again the experimental data remarkably well at all temperatures reported in this figure.

In order to assure that two structures supporting different shear rates coexists in P103 solutions, rheo-optics and SALS measurements under flow were performed. Fig. 11 shows the shear stress versus shear-rate plot and birefringence measurements ($\Delta n'$)

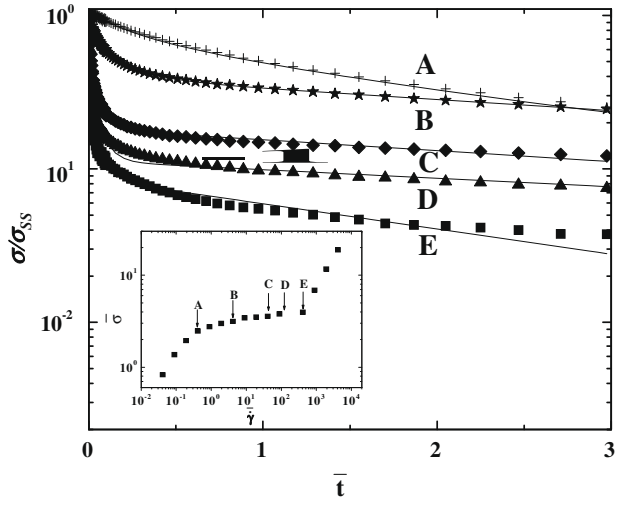

Fig. 9. Normalized stress relaxation after cessation of steady shear flow for a 20 wt% P103 aqueous solution measured at 36 °C and different dimensionless shear rates: (A) 0.415; (B) 4.152; (C) 41.52; (D) 124.56; (E) 415.2. Inset: Dimensionless flow curve for a 20 wt% P103 aqueous solution measured at 36 °C.

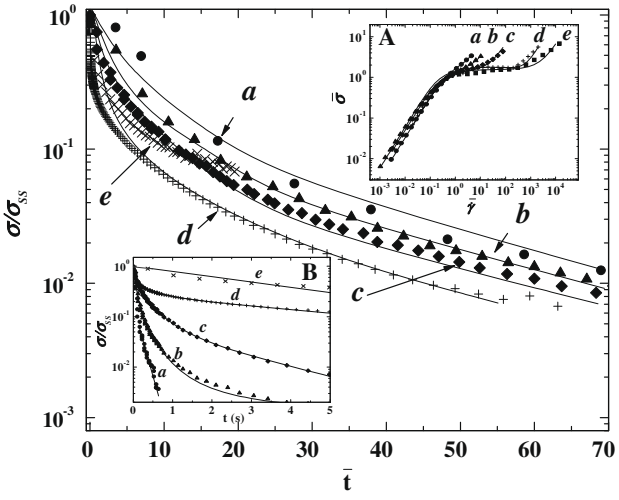

Fig. 10. Normalized stress relaxation after cessation of steady shear flow for a 20 wt% P103 aqueous solution measured at a dimensionless shear rate of 10 and at different temperatures (°C): (a) 32; (b) 33; (c) 34; (d) 35; (e) 38.The solid lines are the predictions of the BMP model. Insets: (A) Dimensionless flow curves for a 20 wt% P103 aqueous solution measured at different temperatures. (B) Normalized stress relaxation after cessation of steady shear flow for a 20 wt% P103 aqueous solution measured at different temperatures.

performed at different shear rates (insets) for a 20 wt% P103 aqueous solution at 36 °C. At low-shear-rates, where the behavior is Newtonian, $\Delta n'$ shows oscillations with small amplitudes and frequencies ($\bar{\dot{\gamma}} = 0.17$). Near $\bar{\dot{\gamma}}_{c1}$, the magnitudes of the oscillations augment ($\bar{\dot{\gamma}} = 0.42$). In the plateau zone where shear banding appears, both the frequency and the amplitude of the birefringence increase and become more erratic as the shear rate increases (insets at $\bar{\dot{\gamma}}$=17, 125, and 415). At very high-shear-rates within the second Newtonian zone, $\Delta n'$ presents oscillations with amplitudes similar to those exhibited in the first Newtonian zone (cf. insets at 0.17 and 2076). The increment of the amplitude of the oscillations indicates that the refraction-index changes are due to the formation of a second phase induced by shear [43].

Fig. 12 shows the steady stress versus shear-rate plot and typical SALS patterns obtained at different levels of shear rate (insets) for a 20 wt% P103 aqueous solution at 36 °C. All SALS patterns were obtained in the velocity–vorticity plane (y, z). Results indicate that the system exhibits three flow regimes. In the quiescent state and in the first Newtonian zone ($\bar{\dot{\gamma}} < \bar{\dot{\gamma}}_{c1} \approx 4.5$), the bright ring indicates that the system structure is isotropic. When the shear rate reaches the first critical value, $\bar{\dot{\gamma}}_{c1}$, the flow of the solution becomes mechanically unstable [33,44–46]. As a result the solution evolves up to a stationary state where bands of a highly sheared liquid of low viscosity coexist with a more viscous part supporting a low-shear-rate (velocity–velocity gradient plane). In the velocity–vorticity plane, a streaked light-scattering pattern appears perpendicular to the vorticity direction and an anisotropic pattern develops parallel to the vorticity direction. When the shear rate increases, the light-scattering streak parallel to the velocity direction diminishes to be completely suppressed when $\bar{\dot{\gamma}}$ reaches the second critical shear rate, $\bar{\dot{\gamma}}_{c2}$. The streaked light-scattering pattern perpendicular to the vorticity direction can be interpreted as shear-induced concentration fluctuations enhanced in the vorticity direction [47], where the density or center of mass of the fluctuations in the flow direction is decoupled from those in the vorticity direction. An evidence is found in the oscillations in $\Delta n\prime(= (n_{\dot{\gamma}} - n_z))$, where the flow birefringence becomes more erratic with small amplitude peaks (inset c in Fig. 12). For $\bar{\dot{\gamma}} = 606\ s^{-1}$, an iso-intensity light-scattering pattern appears, and only a streak perpendicular to the flow is observed. Even though a more detailed analysis of the light-scattering patterns is needed, the intensity of the oscillations suggests a structure length scale in the real space

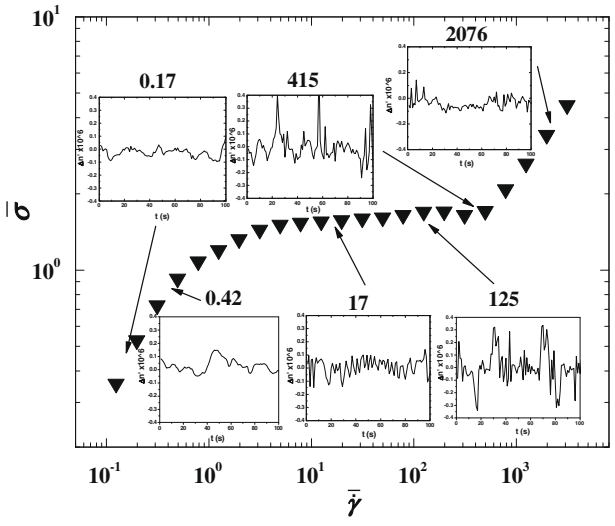

Fig. 11. Dimensionless steady shear flow curve for a 20 wt% P103 aqueous solution at 36 °C. The insets are the flow birefringence ($\Delta n'$) versus time at different dimensionless shear rates.

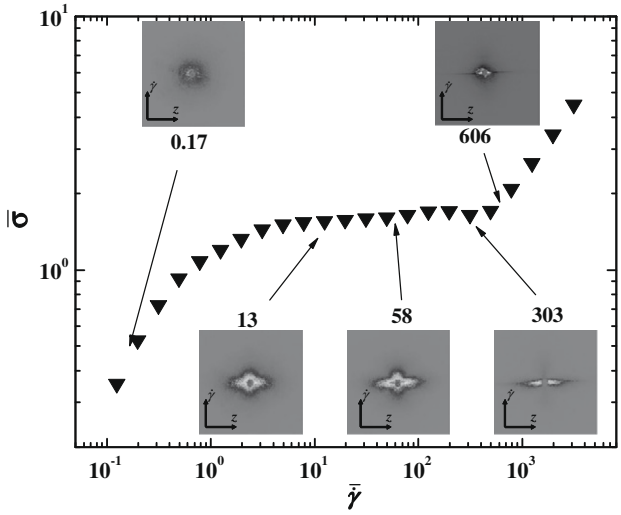

Fig. 12. Dimensionless steady shear flow curve for a 20 wt% P103 aqueous solution at 36 °C. The insets are the SALS patterns obtained at selected dimensionless shear rates.

on the order of micrometers. A detailed analysis will be reported in a forthcoming publication. In the P84 system, Waton et al. [12] using SALS under flow examined the stress plateau region in a narrow temperature and concentration range. Several authors have reported similar streak-like patterns in sheared polymer solutions [48] and blends [49–51], and they have attributed them to the presence of string-like morphology aligned along the flow direction. From $\bar{\dot{\gamma}} = 14$ to 347, light-scattering patterns show strong relative intensities at very small wave vectors, suggesting that in real space, large structures oriented in the flow direction exist. In the second Newtonian region, the light-scattering patterns exhibit an oval halo and a finer streaked ascribed to instabilities arising due to the viscoelasticity of the solutions.

5. Concluding remarks

The rheological properties of the semidilute P103 micellar solutions are highly dependent on temperature, since the shear viscosity and the storage modulus increase nearly three orders of magnitude with increasing temperature (Fig. 2). These changes are related to the spherical-to-worm-like micellar transition, in which the length of the micelles and the entanglement number density augment with increasing temperature. The storage modulus (G') data collapse in a double time–temperature–concentration master curve in the whole concentration and temperature range examined (Fig. 5A). The loss modulus (G'') data also overlap at low frequencies, but they depart at higher reduced frequencies on the order of the inverse of the breaking micellar time and because of the occurrence of Rouse and breathing modes (Fig. 5B) [39].

Curves of the dimensionless stress $\bar{\sigma}$ plotted as a function of the dimensionless shear-rate $\bar{\dot{\gamma}}$ overlap for different concentrations and temperatures up to the onset of the nonlinear behavior (Fig. 6). For samples with concentrations from 15 and to 20 wt%, the stress versus shear-rate curves display a stress plateau in a narrow temperature range similar to that observed in polymer-like micellar solutions of ionic surfactants. Furthermore, overshoots and oscillations that last several scores of relaxation times are detected on inception of shear flow when the applied shear rate is within the two critical shear rates that bound the stress plateau region (Fig. 8); stress relaxation data depict a single relaxation mechanism in the homogeneous Newtonian regions at low and

high-shear-rates, and two main relaxation times in the stress plateau region (Figs. 9 and 10). Birefringence (Fig. 11) and SALS (Fig. 12) measurements under flow indicate that two phases coexists for shear rates in the plateau stress region.

Experimental and theoretical evidence of nonequilibrium critical behavior is presented, in which the order parameter is the difference of the critical shear rates that limit the span of the plateau stress. In particular, an extended irreversible thermodynamics analysis indicates that the dissipation energy versus shear-rate curve exhibits two minima that coincide with the critical shear rates, which approaches each other and become shallower as the stress plateau region shrinks (Fig. 7). In the neighborhood of the disappearance of the stress plateau region, the dissipation energy curve becomes flat, similar to the free energy curve as an equilibrium critical point is approached.

It is important to remark that in polymer-like micellar solutions of ionic surfactants, shear-banding flow is typically observed when the system is in the fast-breaking regime, that is, when the relaxation is controlled by the kinetics of breaking and recombination of the micelles [23,28]. P103 worm-like micelles do not follow Maxwell behavior, which is evident from results depicted in Figs. 3 and 4 and from the departures from the osculating semicircle in Cole–Cole plots (not shown), indicating that the relaxation is diffusion controlled (i.e., τ_{Rep} is similar or larger than τ_{Break}); nevertheless, P103 solutions exhibit shear-banding flow in a narrow temperature–and–concentration range. The comparison of the linear (Fig. 5) and nonlinear (Fig. 6) rheological behaviors, on the other hand, indicates a strong relationship between the departures from the correlation in the G'' data (Fig. 5b) with the extent of the plateau region (Fig. 6). The departures at high frequencies in the loss modulus (Fig. 5B) are related to departures from the osculating semicircle in Cole–Cole plots (G'' versus G') that governs the transition from fast breaking to slow breaking regimes. In the fast-breaking regime (Maxwell-like behavior), linear viscoelastic data describe a semicircle and the nonlinear counterpart describes a wide stress plateau. The departures from the correlation in Fig. 5B occur at higher frequencies on increasing temperature and concentration, and these correspond to a more extended plateau region as depicted in Fig. 6. Likewise, for lower temperatures and smaller concentrations, the departure from the correlation in Fig. 5B occurs at lower frequencies and the nonlinear behavior in Fig. 6 is close to that of a Newtonian fluid, with no plateau. In fact, in polymer-like micellar solutions, the plateau stress becomes smaller as the phase boundary is approached [21,23,28,38]. Under these circumstances, the transition from a fast- to a slow-breaking mechanism should be rather abrupt, just like in the system examined here. Incidentally, Waton et al. [12] reported that worm-like micellar solutions of P84 follow a similar linear and nonlinear rheological behavior that the system examined here, i.e., strong deviations from Maxwell behavior in the linear regime and shear-banding flow in the nonlinear regime.

The BMP model predicts steady state and most of the features of the transient nonlinear rheology in systems where kinetic processes of breakage and reformation occur simultaneously to flow-induced microstructural changes. In particular, the model reproduces quite well steady flow and relaxation after cessation of flow and the occurrence of a nonequilibrium critical point.

Acknowledgments

This work was supported by projects ECOS-Nord M05P02E, MO6-P03 and the National Council of Science and Technology of México (CONACYT Grants 25463 and 47192) and CNRS, France. Two of us (N.T. and J.G.A.) acknowledge the scholarship from CONACYT. Professor J.F.A. Soltero is grateful for the hospitality of the "Laboratoire de Rhéologie" during the time that this research was performed.

References

[1] I.R. Schmolka, in: P.J. Tarcha (Ed.), Polymer for Controlled Drug Delivery, CRC Press, Boston, 1992.
[2] P.-C. Chen-Chow, S.G. Frank, Int. J. Pharm. 8 (1981) 89.
[3] R.K. Prud'homme, G. Wu, D.K. Schneider, Langmuir 12 (1996) 465.
[4] K. Mortensen, J.S. Pedersen, Macromolecules 26 (1993) 805.
[5] K. Mortensen, W. Brown, Macromolecules 26 (1993) 4128.
[6] K. Schillén, W. Brown, R.M. Johnsen, Macromolecules 27 (1994) 4825.
[7] E.B. Jørgensen, S. Hvidt, W. Brown, K. Schilén, Macromolecules 30 (1997) 2355.
[8] B. Michels, G. Waton, R. Zana, Colloids Surf. A 183 (2001) 55.
[9] M. Duval, G. Waton, F. Schosseler, Langmuir 21 (2005) 4904.
[10] Y. Liu, S.-H. Chen, J.S. Huang, Macromolecules 31 (1998) 2236.
[11] V.K. Aswall, P.S. Goyal, J. Kohlbrecher, P. Bahadur, Chem. Phys. Lett. 349 (2001) 458.
[12] G. Waton, B. Michels, A. Steyer, F. Schosseler, Macromolecules 37 (2004) 2313.
[13] W. Brown, K. Schillén, M. Almgren, S. Hvidt, P. Bahadur, J. Phys. Chem. 95 (1991) 1850.
[14] W. Brown, K. Schilliin, S. Hvidt, J. Phys. Chem. 96 (1992) 6038.
[15] P. Bahadur, K. Pandya, Langmuir 8 (1992) 2666.
[16] L. Lobry, N. Micali, F. Mallamace, C. Liao, S.-H. Chen, Phys. Rev. E 60 (1999) 7076.
[17] S. Hvidt, B. Jørgensen, W. Brown, K. Schillén, J. Phys. Chem. 98 (1994) 12320.
[18] E. Eiser, F. Molino, G. Porte, O. Diat, Phys. Rev. E. 61 (2000) 6759.
[19] E. Eiser, F. Molino, G. Porte, X. Pitón, Rheol. Acta 39 (2000) 201.
[20] J.F.A. Soltero, F. Bautista, J.E. Puig, O. Manero, Langmuir 15 (1999) 1604.
[21] J.-F. Berret, in: R.G. Weiss, P. Terech (Eds.), Molecular Gels. Materials with Self-assembled Fibrillar Networks, Springer, Secaucus, 2006.
[22] J.F.A. Soltero, J.G. Álvarez-Ramírez, V.V.A. Fernández, N. Tepale, F. Bautista, E.R. Macías, J.H. Pérez-López, P.C. Shulz, O. Manero, C. Solans, J.E. Puig, J. Colloid Interface Sci. 312 (2007) 130.
[23] J.E. Puig, F. Bautista, J.F.A. Soltero, O. Manero, in: R. Zana, E.W. Kaler (Eds.), Giant Micelles. Properties and Applications, Dekker, Boca Raton, FL, 2007.
[24] J.G. Álvarez-Ramírez, V.V.A. Fernández, E.R. Macías, Y. Rharbi, P. Taboada, R. Gámez-Corrales, J.E. Puig, J.F.A. Soltero, J. Colloid Interface Sci. 333 (2009) 655.
[25] F. Bautista, J.F.A. Soltero, J.H. Pérez-López, J.E. Puig, O. Manero, J. Non-Newt. Fluid Mech. 94 (2000) 57.
[26] F. Bautista, J.F.A. Soltero, E.R. Macías, O. Manero, J.E. Puig, J. Phys. Chem. B 106 (2002) 13018.
[27] O. Manero, J.H. Pérez-López, J.I. Escalante, J.E. Puig, F. Bautista, J. Non-Newt. Fluid. Mech. 146 (2007) 22.
[28] J.I. Escalante, E.R. Macias, F. Bautista, J.H. Pérez-López, J.F.A. Soltero, O. Manero, J.E. Puig, Langmuir 19 (2003) 6620.
[29] E.S. Boek, J.T. Padding, V.J. Anderson, P.M.J. Tardy, J. Crawshaw, J.R.A. Pearson, J. Non-Newt. Fluid Mech. 126 (2005) 39.
[30] B.M. Marín-Santibañez, J. Pérez-Gonzalez, L. de Vargas, F. Rodríguez-Gonzalez, Langmuir 22 (2006) 4015.
[31] B.C. Blakey, D.F. James, Int. J. Miner. Proc. 70 (2003) 23.
[32] F. Bautista, J.H. Pérez-López, J.P. García, J.E. Puig, O. Manero, J. Non-Newt. Fluid Mech. 144 (2007) 160.
[33] J.-F. Berret, G. Porte, J.P. Decruppe, Phys. Rev. E. 55 (1997) 1668.
[34] J.M. Piau, M. Dorget, J.F. Palierne, A. Pouchelon, J. Rheol. 43 (1999) 305.
[35] F. Pignon, A. Magnin, J.M. Piau, Phys. Rev. Lett. 79 (1997) 4689.
[36] F. Pignon, A. Magnin, J.M. Piau, J. Rheol. 42 (1998) 1349.
[37] M.E. Cates, S. Fielding, in: R. Zana, E.W. Kaler (Eds.), Giant Micelles. Properties and Applications, Dekker, Boca Raton, FL, 2007.
[38] J.D. Ferry, Viscoelastic Properties of Polymers, Wiley, New York, 1980.
[39] R. Granek, M.E. Cates, J. Chem. Phys. 96 (1992) 4758.
[40] J.-P. Decruppe, E. Cappelare, R. Cresseley, J. Phys. II 7 (1997) 257.
[41] J.-F. Berret, G. Porte, Phys. Rev. E. 60 (1999) 4268.
[42] J.-F. Berret, D.C. Roux, G. Porte, J. Phys. II 4 (1994) 1261.
[43] S. Lerouge, J.-P. Decruppe, J.-F. Berret, Langmuir 16 (2000) 6464.
[44] M.E. Cates, T.C.B. McLeish, G. Marrucci, Europhys. Lett. 21 (1993) 451.
[45] M.E. Cates, J. Phys. Condens. Matter 8 (1996) 9167.
[46] J.F. Berret, D.C. Roux, G. Porte, P. Lindner, Europhys. Lett. 25 (1994) 521.
[47] E. Helfand, G.H. Fredrickson, Phys Rev. Lett. 62 (1989) 2468.
[48] T. Kume, T. Hashimoto, T. Takahasgi, G.G. Fuller, Macromolecules 30 (1997) 7232.
[49] M.L. Fernandez, J.S. Higgins, M. Richards, Polymer 36 (1995) 931.
[50] M.S. Kim, K. Levon, Eur. Polym. J. 33 (1997) 1787.
[51] L. Kielhorn, R.H. Colby, C.C. Han, Macromolecules 33 (2000) 2486.